

PACS numbers: 62.20.Qp, 62.25.-g, 68.65.Ac, 81.15.-z, 81.40.Pq, 81.65.Kn, 81.65.Mq

## Arc-Evaporated Nanoscale Multilayer Nitride-Based Coatings for Protection Against Wear, Corrosion, and Oxidation

A. D. Pogrebnyak<sup>\*</sup>, O. M. Ivasishin<sup>†</sup>, and V. M. Beresnev<sup>‡</sup>

<sup>\*</sup>*Sumy State University,  
2 Rymsky-Korsakov Str.,  
UA-40007 Sumy, Ukraine*

<sup>†</sup>*G. V. Kurdyumov Institute for Metal Physics, N.A.S. of Ukraine,  
36 Academician Vernadsky Blvd.,  
UA-03680 Kyiv, Ukraine*

<sup>‡</sup>*V. N. Karazin Kharkiv National University,  
4 Svobody Sq.,  
UA-61000 Kharkiv, Ukraine*

The studies of the structure and properties of nanoscale multilayer coatings based on the nitrides of refractory metals are summarized in a brief review. By the example of TiN/MoN, TiN/ZrN, CrN/MoN, and more complex (multilayer) (TiZrNbTaHf)N/WN:(TiZrNbTaHf)N/MoN obtained by vacuum-arc deposition of cathode, the dependences of their hardness, wear resistance, friction, corrosion, and oxidation on conditions of the deposition and layers' thickness are investigated and analysed. The regularities of the structure and behaviour properties of such nanoscale multilayer coatings depending on the size of nanograins, textures, and stresses arising in these coatings are described.

У короткому огляді узагальнено результати досліджень структури та властивостей наномасштабних багат шарових покриттів нітридів тугоплавких металів. На прикладі TiN/MoN-, TiN/ZrN-, CrN/MoN- та більш складних (багат шарових) (TiZrNbTaHf)N/WN:(TiZrNbTaHf)N/MoN-покриттів, одержаних методом вакуумно-дугового осадження катоду, досліджено та проаналізовано залежності їх твердості, зносостійкості, тертя, корозії й окиснення від умов осадження та товщини шарів. Відмічено закономірності структури та властивостей поведінки даних наномасштабних багат шарових покриттів від розміру нанозерен, текстури та напруг, що виникають у цих покриттях.

В кратком обзоре обобщены результаты исследований структуры и свойств наномасштабных многослойных покрытий нитридов тугоплавких металлов. На примере TiN/MoN-, TiN/ZrN-, CrN/MoN- и более сложных (многос-

слоиных) (TiZrNbTaHf)N/WN:(TiZrNbTaHf)N/MoN-покрытий, полученных методом вакуумно-дугового осаждения катода, исследованы и проанализированы зависимости их твёрдости, износостойкости, трения, коррозии и окисления от условий осаждения и толщины слоёв. Отмечены закономерности структуры и свойств поведения таких наномасштабных многослойных покрытий от размера нанозёрен, текстуры и напряжений, возникающих в этих покрытиях.

**Keywords:** nanoscale nanocomposite coatings, structure, wear, corrosion resistance, hardness.

**Ключові слова:** нанорозмірні нанокompatитні покриття, структура, зношування, антикорозійна стійкість, твердість.

**Ключевые слова:** наноразмерные нанокompatитные покрытия, структура, износ, антикоррозийная стойкость, твёрдость.

*(Received January 19, 2016)*

## 1. INTRODUCTION

One of the most promising applications of nanomaterials is the creation of protective coatings for products and tools with different functional purposes. Such material characteristics as hardness, elasticity, adhesive and cohesive strength, durability, thermal and chemical stability and others are particularly important in this regard [1–15].

Results of scientific researches show the tendency of active use of nitrides and borides of transition metals and their combination in the development of protective materials [16–25]. While nitrides of single elements are studied well enough, their multilayer modifications need study that is more detailed [26–35]. Therefore, the study of features of structure, elemental and phase composition of multilayer coatings depending on the deposition conditions is an important task in solid-state physics and materials science [36–51].

## 2. RESULTS AND DISCUSSIONS

### 2.1. TiN/ZrN Coatings

We clearly see layers with cubic TiN and ZrN phases (of the NaCl structure type) without preferred orientation of crystallites in the surface layers. Increasing of the  $\lambda$  period led to increasing of the TiN layers specific contribution. It is seen from the changes in the intensity of the peaks of TiN and ZrN phases (see Fig. 1). Increasing of the deposition time and, as a result, bilayer thickness as well as total period of the multilayer system led to changes of the lattice period of nitride

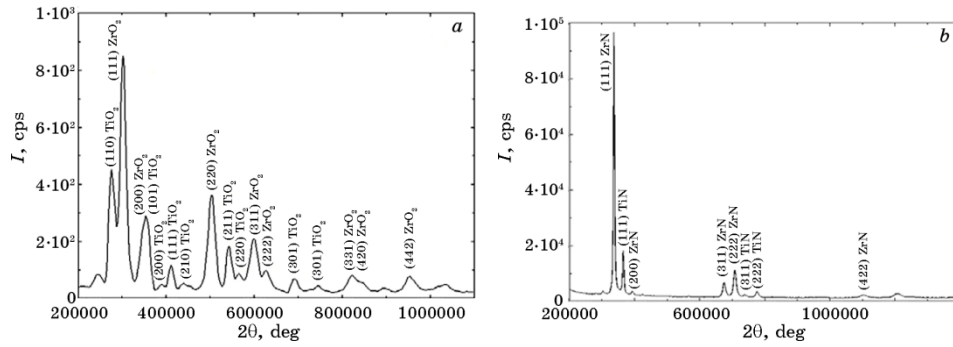


**Fig. 1.** Diffraction patterns of the TiN/ZrN coatings ( $\lambda \approx 70$  nm) after thermal annealing under the temperature of  $700^\circ\text{C}$  for one hour: *a*—from the surface without polishing, *b*—after polishing of the oxidized surface on the depth of  $5 \mu\text{m}$  [15].

phases in the layers. Lattice period decreased with increasing of the TiN-layers' thickness from  $0.4241502$  nm (deposition time was 20 sec,  $\lambda \approx 70$  nm) to  $0.4238870$  nm (deposition time was 40 sec,  $\lambda \approx 250$  nm). Changes for ZrN layers were not so large: from  $0.4581055$  nm (deposition time—20 sec) to  $0.4581046$  nm (deposition time was 40 sec).

Annealing in the oxygen atmosphere led to oxidation of the surface layers [19, 20] and to forming of dioxides as the main phases:  $\text{TiO}_2$  (with tetragonal rutile-type crystal system; basic, up to 95 vol.% in the layers based on titanium) and anatase (5 vol.% and less). We can determine anatase (DB card number 5000223) on the diffraction spectra (Fig. 1, *a*) using the most strong first line on the angle  $2\theta \approx 25.36$  degrees. Diffraction spectrum is shown for the rutile (DB card number 9007531) (see Fig. 1, *a*). Only one type of dioxide  $\text{ZrO}_2$  (arkel having a cubic crystal system, DB card number 5000038) was formed in the zirconium nitride layers after oxidation.

Layered X-ray analysis showed that after removal of the surface layer (thickness of about 5 microns) by polishing, we could see dioxides only in the subsurface layer of the coating. In more thick layers (Fig. 1, *b*), we did not find oxides whereas nitrides are characterized by preferred orientation of crystallites with the [111] axis, perpendicular to the plane of growth. Therefore, preferred orientation with the [111] axis was formed at the beginning stage of growth for both TiN and ZrN crystallites. Increasing of the total thickness of the coatings and relaxation of the compressive stresses led to disorientation of crystallites, *i.e.* preferred orientation was not observed.

Using XRD analysis data (Fig. 1), we could assume that due to disorientation of crystallites in the surface layers and low compressive stresses, oxygen from the atmosphere penetrates into the subsurface layers during deposition. It formed stable dioxide phases of metals due

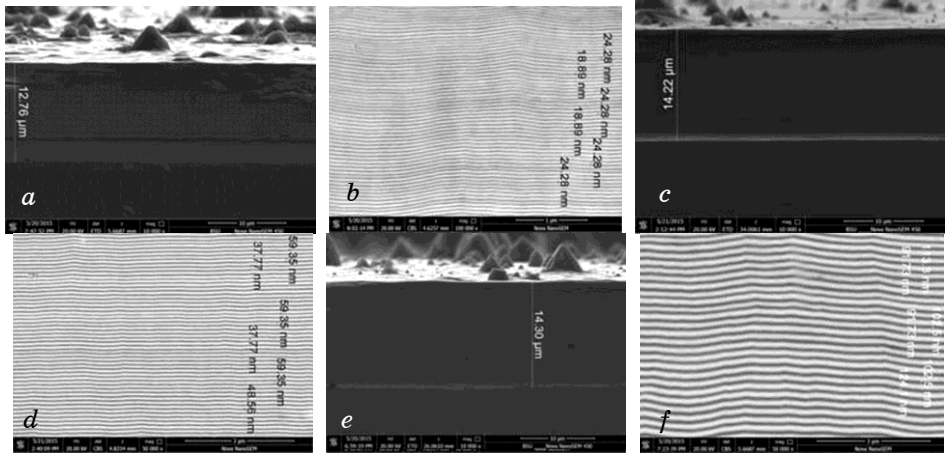


**Fig. 2.** Electron images of the cross-sections of the TiN/ZrN samples (general view of the cross-section and magnified fragment) with amount of layers 533 (*a* and *b*), 233 (*c* and *d*) and 134 (*e* and *f*) [15].

to easier diffusion by intercrystallite ways. In more deep layers corresponding to the beginning stages of growth, [111] texture of growth appeared due to compressive stresses [7, 8]. This texture prevents diffusion of oxygen into such layers due to high packing density of the plane (111), so there is not enough oxygen to form dioxide phases.

Transmission electron microscopy (TEM) allowed providing detailed analysis of changes in the surface layers after oxidation. Electron images of the cross-sections of the TiN/ZrN samples from different series are presented in Fig. 2. Good planarity was observed even for the thinnest layers of the coatings from the first series (Figs. 2, *a* and *b*). High continuity of the coatings and the lack of inhomogeneity, such as droplet fractions, are also typical for investigated samples.

Comparison of electron microscopy images of the structural state of the layers in the multilayer TiN/ZrN coatings with total amount of layers 134 (Fig. 3) showed that increasing of the volume fraction led to bending of layers, stratification with separation and loss of strength during oxidation (Figs. 3, *c* and *d*). We observed dome-like discontinuities in the areas of partial separation of layers (Fig. 3, *d*) on the surface. Comparison of structures 1 and 2 in Fig. 3 showed that main volume changes took place in the titanium-based layers, whose thickness increased from 80 nm to 110 nm, *i.e.* by 37.5%. Thickness of zirconium-based layers increased from an average value 120 nm before annealing to 135 nm after annealing during oxidation (Figs. 3, *a* and 3, *c*), *i.e.* by 12.5%. Wherein, columnar character of the grain structure is clearly seen in zirconium-based layers, that is why they become quite fragile. High density was observed in titanium-based layers, so we can

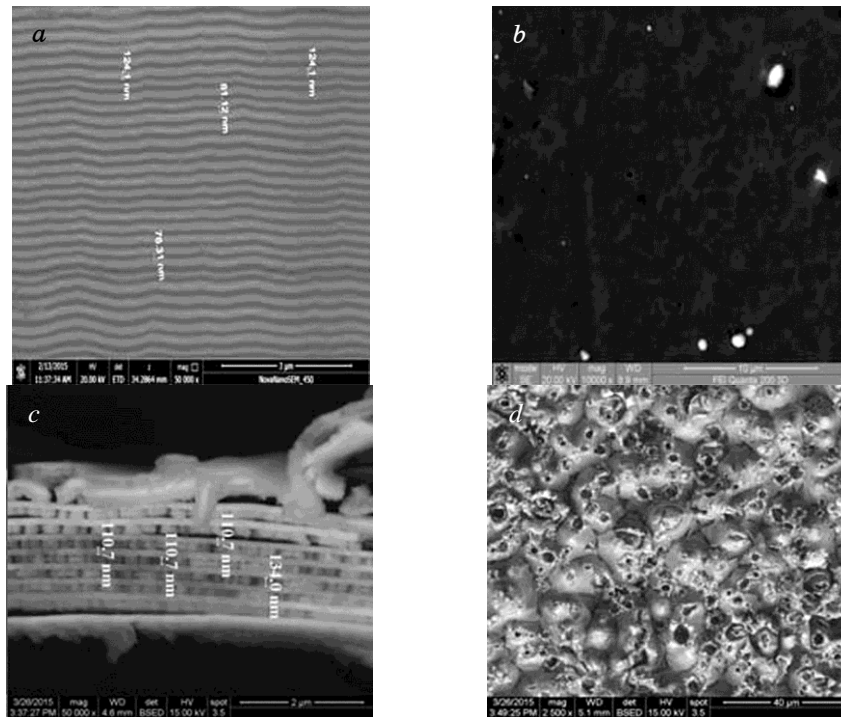


**Fig. 3.** Image of the cross-section and surface of the coating of the third series before (a, b) and after (c, d) annealing [15].

assume that these layers are subjected to compression and compaction because of oxidation, despite the relatively high increasing of the thickness. Thus, compensating tensile strain in the layers of the plane of growth should be created in titanium-based layers, which determines their tendency to brittle fracture. Interphase boundary is the main area of separation. It can be explained by decreasing of the adhesive bonds during forming of phases with different crystal lattices (cubic in zirconium-based layers and tetragonal in titanium-based layers) due to oxidation.

Thus, unlike single-layer coating or coating with few layers, only subsurface layers are susceptible to phase changes (in multilayer coating with amount of nanoscale layers more than 100) even in the case of severe operation conditions in active oxygen atmosphere, thereby preventing main structural state of inner carrier layers from changes.

Hardness is well known as a universal characteristic, which allow rapidly estimating of mechanical properties of the coatings [8]. We defined harness using microindentation method, and hardness was around  $H \approx 42$  GPa for the first series of samples,  $H \approx 38$  GPa and  $H \approx 36$  GPa for the second and the third series of samples accordingly.

**TABLE 1.** Tribological properties of the multilayer TiN/ZrN coatings.

Series No.	Friction Coefficient		Wear factor, $\text{mm}^3 \times \text{N}^{-1} \times \text{mm}^{-1}$	
	Starting moment	During tests	Counterbody ( $\times 10^{-3}$ )	Samples ( $\times 10^{-5}$ )
1	0.59	1.0	1.9	1.3
2	0.62	1.2	2.0	1.5
3	0.62	1.1	2.2	1.4

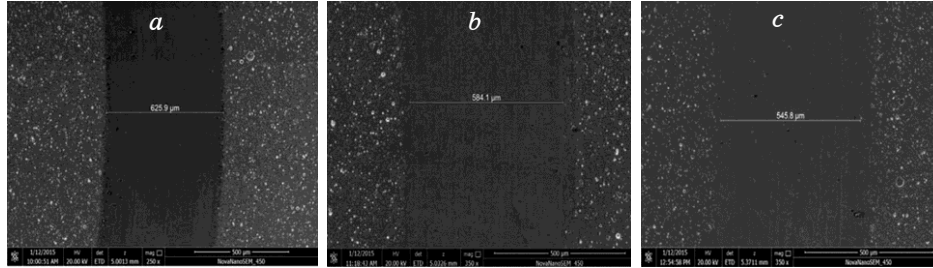
Thus, high hardness is typical for all series of samples with different bilayer thickness, so such coatings are perspective for using as protective ones. In this connection, it was also necessary to provide tribological tests to determine basic mechanical properties upon contact of the coating with counterbody.

Results of tribological tests of multilayer samples with different bilayer thickness under room temperature are presented in Table 1. It is clearly seen from the table, that fabricated multilayer coatings have high wear coefficient paired with  $\text{Al}_2\text{O}_3$  counterbody.

Figure 4 shows the images of friction tracks for TiN/ZrN samples with different bilayer thickness.

One could see that friction tracks are characterized by absence of burrs, cleavages and radial cracks, indicating the high quality and adhesive strength of coatings.

All fabricated coatings have good wear resistance average values of the reduced wear were  $(1.3-1.5) \cdot 10^{-5} \text{ mm}^3 \times \text{N}^{-1} \times \text{mm}^{-1}$ . Wear of the counterbody was rather small  $(1.9-2.2) \cdot 10^{-6} \text{ mm}^3 \times \text{N}^{-1} \times \text{mm}^{-1}$ . Chipping, cracking and peeling of coatings were not observed during friction tests. We found good adhesion of the coatings to substrates. There were no plastic deformation during tests; the observed wear is rather typical for soft metals [5, 6].

**Fig. 4.** Friction tracks of the multilayer TiN/ZrN coatings: sample of the first (a), second (b), and third (c) series [15].

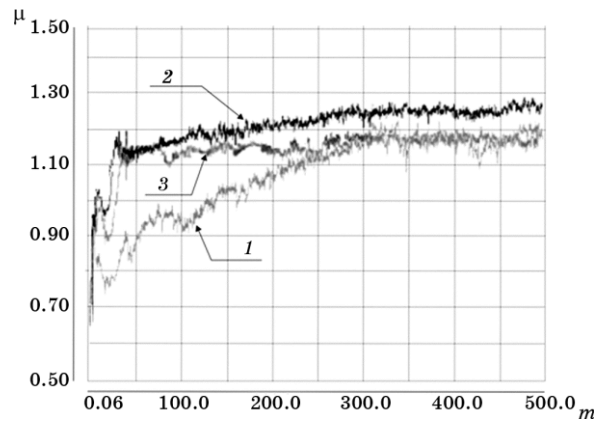


Fig. 5. Friction coefficients of the TiN/ZrN coatings: samples of the first (1), second (2), and third (3) series [15].

Figure 5 shows values of friction coefficients for multilayer TiN/ZrN coatings. Samples from the second series had the highest values of the friction coefficient  $\mu$  (curve 2 in Fig. 5). There was a great difference between values of friction coefficient for the first and third series on the distance from 0 to 300 meters. Friction coefficient  $\mu$  for the samples from the third series sharply increased to the value 1.2 and stayed on this level along the length of testing area. Values of  $\mu$  for the samples of the first series monotonically increase along the friction distance and are equal to the values for the third series. Friction coefficient of the samples from the second series sharply achieved the value 1.2 and then slowly monotonically increased to the value 1.3.

Friction coefficient  $\mu$  significantly depended on bilayer thickness and total thickness of the coatings. The lowest friction coefficient was observed for the samples from the first series with 20 nm bilayer thickness and  $\lambda \approx 40$  nm. The highest values of friction coefficient were observed for the samples of the second series with  $\lambda \approx 70$  nm.

## 2.2. TiN/MoN Coatings

Multilayer nanostructured TiN/MoN coatings were fabricated using vacuum arc evaporation of two cathodes at atmosphere of molecular nitrogen. For this procedure, we used unit ‘Bulat-6’, which allows obtaining coatings both for scientific purposes and for industry. Substrate holder rotatable at predetermined speed allows alternating deposition of titanium and molybdenum nitrides layers from two diametrically arranged evaporators [16]. Thus, it is possible to obtain coatings with different elemental and structural-phase compositions by adjusting the current and voltage of the substrate and cathodes, ni-

**TABLE 2.** Parameters of multilayer TiN/MoN deposition.

Sample	Period $\lambda$ , nm		$t_{\text{layer}}$ , s	$I_{\text{dep}}$ , A	$I_{\text{bias}}$ , A	$U_{\text{bias}}$ , V	$f$ , kHz	$P_{\text{N}}$ , Pa
	Expected	Measured						
No. 1	4	8	2	95–100	0.8	–40	7	0.5
No. 2	4	8						
No. 3	20	25	10	95–100	0.9	–40	7	0.5
No. 4	20	25						
No. 5	40	50	20		0.9	–40		
No. 6	80	100	40		1.0	–40		

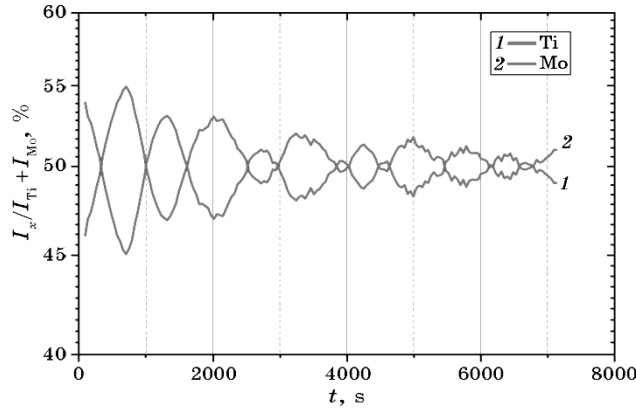
trogen pressure in the chamber and other parameters. The deposition parameters are located in Table 2.

Because of deposition of samples, the multilayer coatings with various thicknesses of the individual layers from 8 nm to 100 nm were prepared. The total coating thickness was reached 8.4 microns.

If we consider the presence of only two elements, Mo and Ti, we get the data shown in Fig. 6. The alternation of TiN and MoN layers is traced quite well in this graph. Unfortunately, surface roughness and relief layers of coating make it difficult to separate the layers more clearly by SIMS analysis.

Used parameters of depth profile analysis for sample No. 4 lead to sputtering rate of 2.0 nm/min for  $\text{SiO}_2$ . Due to the roughness, we did not measure the crater depth with stylus profilometer.

In order to estimate the sputtering rate of TiN/MoN, we carried out SRIM simulations (see Table 3). It is most likely that the sputtering

**Fig. 6.** SIMS depth profile analysis of normalized secondary ion currents:  $m/z = 48$  ( $\text{Ti}^+$ ) and  $98$  ( $\text{Mo}^+$ ) [16].

**TABLE 3.** Parameters of SIMS analysis and SRIM simulations.

500 nA, 1.72 keV Ar <sup>+</sup> primary ion beam at 45° incidence angle			
Material	SiO <sub>2</sub>	TiN	MoN
S* (atoms/ion)	3.46	3.27	4.37
Ion range* (nm)	4.4	3.3	2.7
Sputtering rate (nm/min)	2.0	—	—

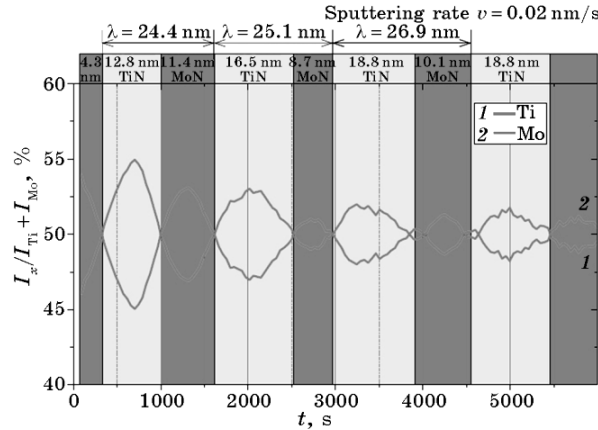
\*Values obtained from SRIM simulation.

rate of TiN and MoN was lower than for SiO<sub>2</sub> (lower than 2.0 nm/min). Having compared results of SRIM simulation with data obtained from RBS spectra and SEM images of the cross-section of multilayer samples, we assumed that the average sputtering rate was about 1.1–1.3 nm/min (or  $\cong 0.02$  nm/s).

The depth profile analysis was carried out for five hours. The crater of 2.5×2.5 mm was sputtered during this time. Taking the sputtering rate of 0.02 nm/s as a basis, it is possible to determine that crater depth was 360–400 nm. Figure 7 shows a modernized previous graph with the calculated thicknesses of the first few layers from the surface of TiN/MoN coating.

XRD patterns of TiN/MoN multilayer coatings with double layer thickness of  $\lambda = 25, 50, 100$  nm are shown in Fig. 3, *a*. Main peaks are located around  $2\theta = 36.5^\circ$  and  $2\theta = 42.5^\circ$ . A more detailed study of the spectral lines gave it possible to detect the asymmetric shape of the peaks.

Peaks found at  $2\theta = 42.5^\circ$  can be divided into two components, which correspond to (200) f.c.c. TiN and (200) cubic  $\gamma$ -Mo<sub>2</sub>N planes (see Fig.

**Fig. 7.** Determination of the coating layers based on SIMS analysis [16].

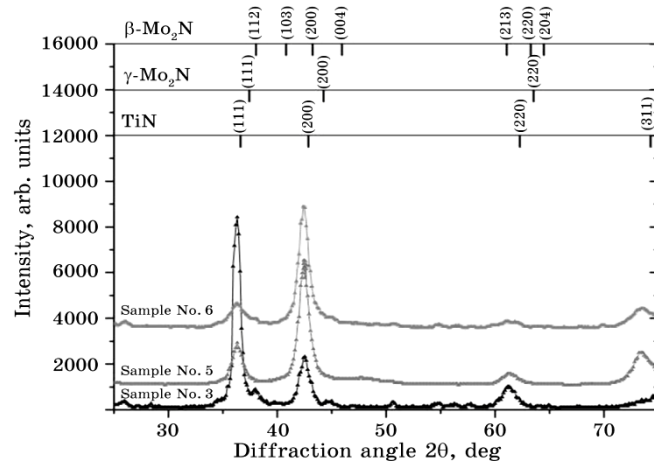


**Fig. 8.** The diffraction patterns (XRD), obtained for coatings with different layer thickness  $\lambda = 25, 50$  and  $100$  nm [16].

8). The peak at  $2\theta = 36.5^\circ$  is attributed to (111)-oriented TiN and  $\gamma$ - $\text{Mo}_2\text{N}$  grains. The volume fractions of TiN and  $\gamma$ - $\text{Mo}_2\text{N}$  phases were extracted from the XRD line fitting procedure of the (200) and (111) peaks using the ‘New\_profile’ software.

All of the identified peaks are marked in Fig. 9. These results show that TiN/MoN coatings consist of highly textured (200) cubic layers.

X-ray analysis shows the formation of only one phase with the f.c.c. lattice (structural type NaCl) in coating with  $\lambda = 8$  nm when substrate voltage is  $-40$  V. The formation of two-phase system of TiN with NaCl-

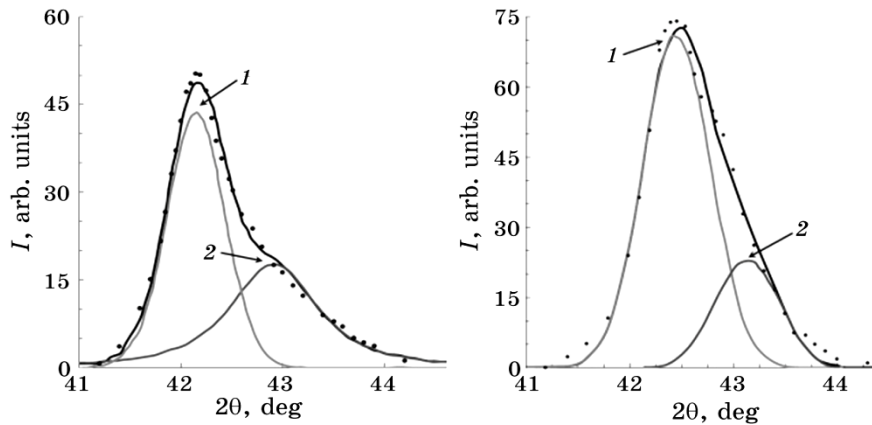


**Fig. 9.** The separation of diffraction spectra into components peaks from the two phases: curve 1—TiN (200), curve 2— $\gamma$ - $\text{Mo}_2\text{N}$  (200). Left—sample #5, right—sample #6 [16].

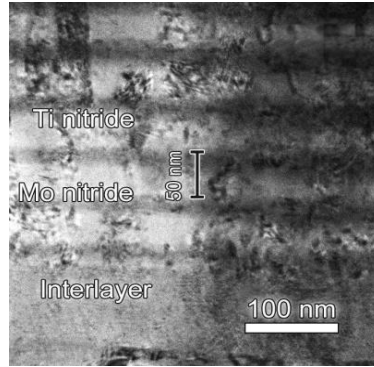


**Fig. 10.** Cross-section TEM bright field image for sample #5 with  $\lambda = 50$  nm [16].

type f.c.c. lattice and high-temperature  $\gamma$ - $\text{Mo}_2\text{N}$  is observed when substrate voltage is increasing to  $-230$  V. The volumetric ratio of TiN/ $\gamma$ - $\text{Mo}_2\text{N}$  phases is 90/10 accordingly.

The presence of only one phase at  $U_b = -40$  V can be explained by the alleged epitaxial growth of thin layers, which growth period is determined by stronger bonds in TiN layer. Increasing of substrate potential to  $-230$  V leads to the appearance of two-phase because of intensification of ion bombardment, which contributes to the grain refinement and the beginning of interfaces formation. Formation of separate layers  $\text{Mo}_2\text{N}$  with a cubic lattice and the appearance of interphase boundaries lead to growth of stress in the TiN phase and increase lattice period in unstressed section. The structure of these coatings is columnar.

Figure 10 shows TEM dark field image (sample No. 5), which demonstrates columnar growth in multilayer nitride. It starts from interface between textured (111) steel substrate and TiN/MoN layers. Coating has a 100 nm thin interlayer. According to the data, it consists of Ti, Mo, C and traces of N.

Measurements of hardness and elasticity modulus of most samples were conducted to determine their mechanical properties and ability to durability. A more detailed study of hardness and elasticity are given for samples No. 5 and No. 6 in Fig. 11. They show typical regularities of  $H(L)$  and  $E(L)$ . In measurements, the indenter has reached a depth of coverage almost  $3 \mu\text{m}$ . Penetration of the indenter was almost linear on the whole stage of load application.

Results of hardness and elasticity modulus measurements for coatings with different layer thicknesses are shown in Table 4. As seen, the hardness of the samples tends to decrease with growth of period  $\lambda$  in the coating. The maximum value of hardness,  $H = 47$  GPa, was achieved at the minimum of the resulting coatings period  $\lambda = 8$  nm. Modulus of elasticity changed with changing the thickness of the dou-

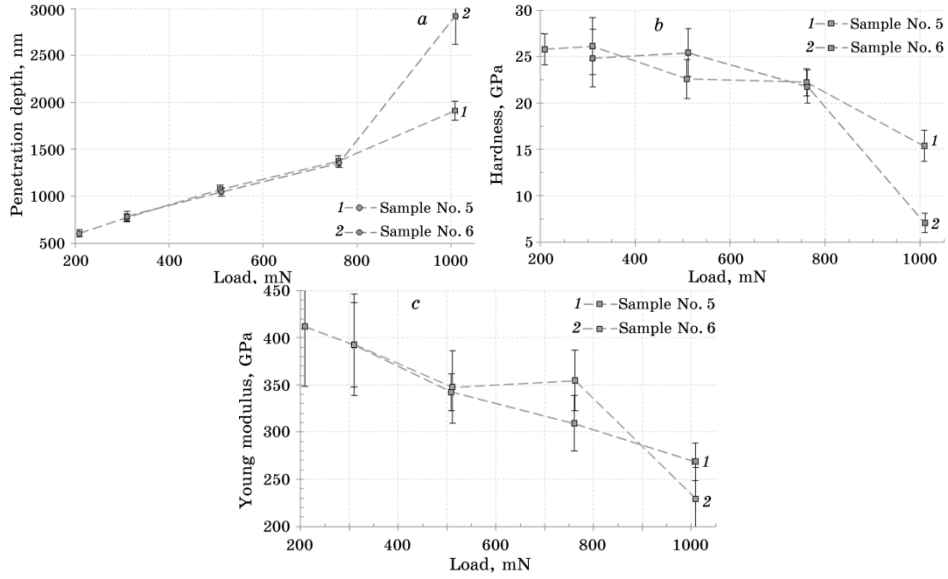


**Fig. 11.** Physical and mechanical properties of coatings: dependence of the penetration depth on the load (a), the hardness on the load (b), and the Young modulus on the load (c) [16].

ble layer. The maximum value of  $E = 470$  GPa was obtained at the same period  $\lambda = 8$  nm.

However, knowing the values of hardness or elasticity of the material is not sufficient to predict its protective capacity. The graph is shown in Fig. 12, where area is divided into sections: 1—section with  $H/E < 0.1$ , which has no good plasticity of the material, 2—section with good plasticity of the material. As can be seen, the sample No. 2 with  $\lambda = 8$  nm is flagged exactly on the line of plasticity.

The general trend of graph testifies to expediency of the studied multilayer TiN/MoN coatings at  $\lambda \leq 8$  nm and at other thicknesses of layers.

These data indicate a good chance of producing TiN/MoN coatings with high plasticity and, hence, the wear resistance.

**TABLE 4.** Hardness and elasticity modulus measurements.

$\lambda$ , nm	$H$ , GPa	$E$ , GPa	$H/E$
8	47	470	0.1
25	31.8	456	0.07
50	26.5	418	0.063
100	25.4	392.6	0.065

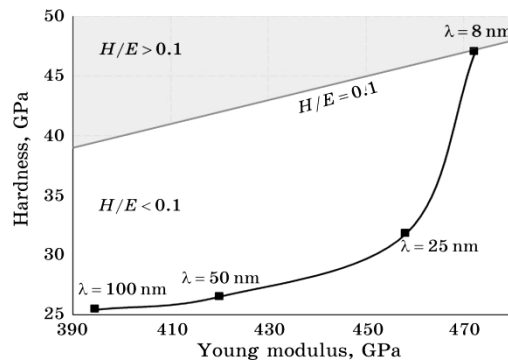


Fig. 12. Characteristics of coatings plasticity [16].

### 2.3. MoN/CrN Coatings

As seen from the side cut area, a multilayer coating (Fig. 13) differs with a sufficiently high planarity of layers and the absence of drop phase in the interior areas of the coating.

The results of elemental analysis show that for small thicknesses, when the layers are the thinnest and the most significant portion of time during precipitation have goes for high-speed rotation of the surface and interaction with residual gases in the working chamber; the depletion of the layers of the coating with light nitrogen atoms (Fig. 14) occurs.

It should be noted that at thicknesses greater than 50 nm, the content of elements in the coating comes to values close to constant, and at a pressure of  $3 \cdot 10^{-3}$  Torr makes a proportion close to 1 between the metal atoms, and about 33% of nitrogen, which corresponds to the stoichiometry of the phases  $\text{Me}_2\text{N}$  (where Me are metal atoms: Mo or Cr). At a lesser pressure of  $7 \cdot 10^{-4}$  Torr and  $2.4 \cdot 10^{-4}$  Torr, the nitrogen contents drops sharply to 17.09 and 6.33 at.%, respectively.

Analysis of diffraction spectra of the coatings shows that in the case of a small value of the negative bias potential applied to the substrate during the deposition ( $-20$  V) in the spectra (Fig. 15) for all the layer thicknesses in the range of 5–200 nm, phases with cubic lattices based

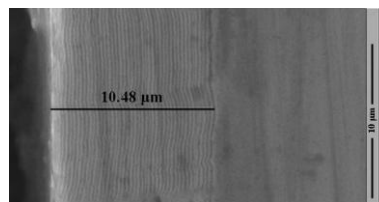
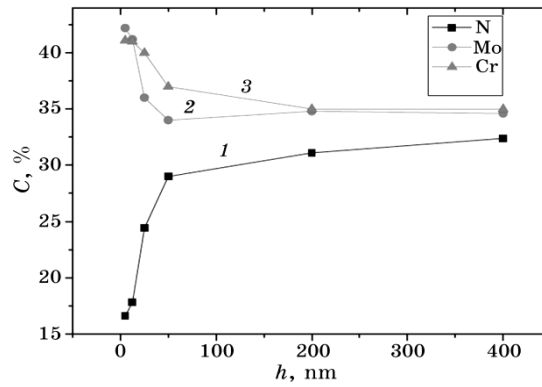


Fig. 13. The image of multilayer coating [17].



**Fig. 14.** Dependence of the content of atoms of nitrogen (1), molybdenum (2), and chromium (3) on the thickness of the layers of the multilayer composite material MoN/CrN [17].

on f.c.c. one with a weak texture with the axis [311], typical for given regimes in monolayer state for  $\gamma$ -Mo<sub>2</sub>N phase [21].

Increasing the bias potential to  $-150$  V and  $-300$  V leads to formation of texture with [100] axis in the layers and to increase in its intensity with increasing the thickness of the layer.

On a substructural level at the lowest  $U_b = -20$  V with the increase of thickness of the layer, the growth of the average crystallite size and nonmonotonic microstrain behaviour are observed: from high values (1.5%) with a layer thickness of less than 20 nm, through a minimum (1.1%) at  $h \approx 100$  nm to 1.4% at large thicknesses (see Fig. 16, a).

With an increase of  $U_b$  up to  $-150$  V in the absolute magnitude, a decrease in microstrain in the layers both by absolute value (0.8–1.05%),

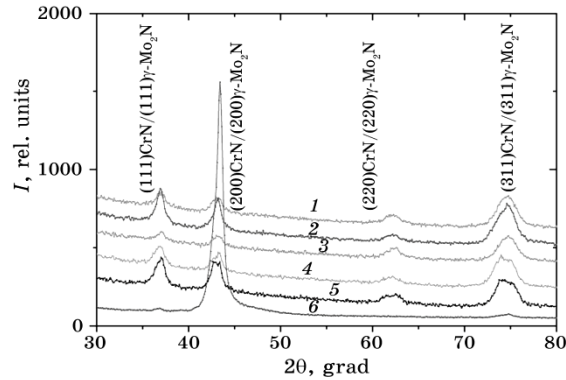


**Fig. 15.** Areas of diffraction spectra of the coatings obtained at  $P_N = 3 \cdot 10^{-3}$  Torr and  $U_b = -20$  V at thickness of the layers of 6 nm (1), 13 nm (2), 25 nm (3), 50 nm (4), 200 nm (5) and  $U_b = -300$  V at thickness of the layers of 13 nm (6) [17].

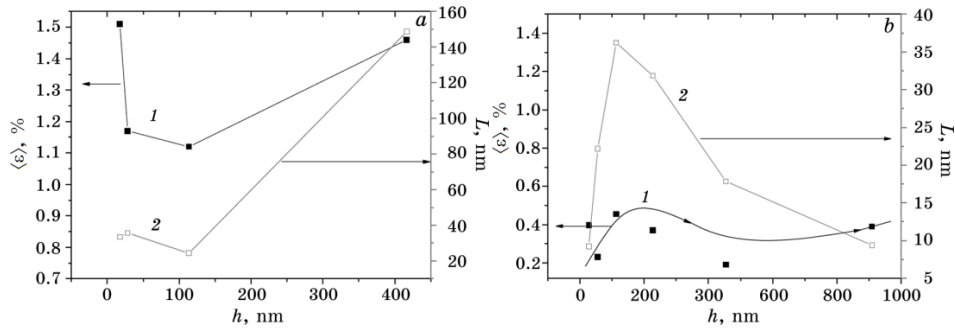


**Fig. 16.** Dependence of substructural characteristics (microdeformation  $\langle \varepsilon \rangle$  (1) and the size of crystallites  $L$  (2)) on the thickness of the layers in the coatings obtained at  $U_b = -20$  V (a) and  $U_b = -300$  V (b) [17].

and by amplitude takes place.

The average crystallite size was varied nonmonotonically, increasing proportionally to the thickness of the layer to a thickness of 100 nm, and then was reduced by 40% with a further increase of the layer thickness.

For highest  $U_b = -300$  V used in paper, the value of microstrain in the layers did not exceed 0.4% (see Fig. 17, b), and the crystallite size was the smallest of the considered for the respective thicknesses. The observed decrease in microdeformation indicates on recombination processes stimulated by higher density of radiation defects along with the increase of the mean energy of the film-forming particles because of increase of  $U$ . The decrease of the average size of crystallites can be linked with the intense action of the defects, which increases the growth of centres of formation.

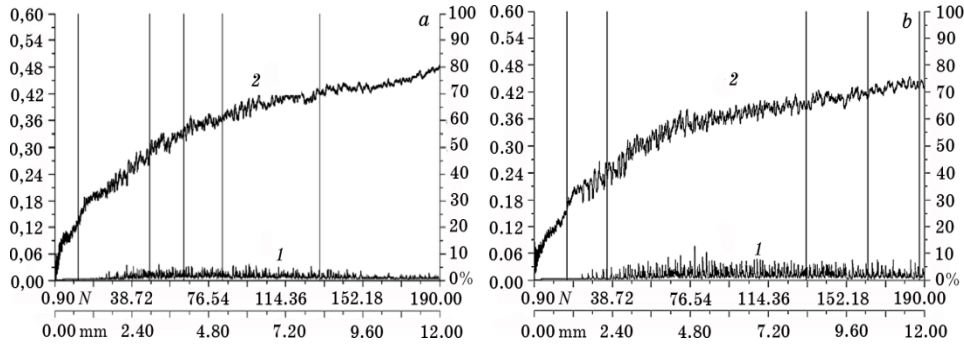


**Fig. 17.** Change in the average values of the amplitude of the acoustic emission (spectrum 1, right scale) and the coefficient of friction (spectrum 2, left scale) for the coatings produced at  $P_N = 3 \cdot 10^{-3}$  Torr and  $U_b = -300$  V at the thickness of the layers 13 nm (a) and 400 nm (b) [17].

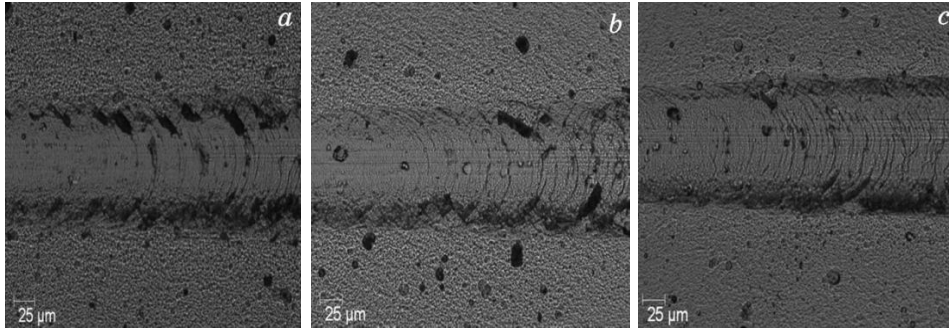


**Fig. 18.** Wear tracks at critical loads,  $L_{C1}$ , for the coatings produced at  $P_N = 3 \cdot 10^{-3}$  Torr and  $U_b = -300$  V at layer thicknesses: 400 nm (a), 200 nm (b), 13 nm (c) [17].

The smaller size of the crystallites and hence a larger average specific volume of the borders defines a higher relaxation capacity for the randomly formed dislocation defects, which define microstrain.

The presence of a small microdeformation and grain size of crystallites may be factors of increasing the adhesive strength of the material. Thus, for adhesive strength tests, the coatings obtained at  $U_b = -300$  V with different layer thicknesses were chosen.

The conducted studies have shown that for the entire range of the used thicknesses of the layers, the uniform wear of the coating over the entire range of applied loads takes place in the composite coatings; this is manifested in the homogeneity of acoustic emission spectrum (see Fig. 17, spectrum 1). Along with this, the coefficient of friction for all the thicknesses of the coatings is sufficiently close and is in the range of 0.18–0.24 (see Fig. 17, spectrum 2).

Along with this, the nature of wear with the decrease of the thickness of the layers becomes more uniform that is especially evident at the areas of the first critical load  $L_{C1}$  (see Fig. 18). This indicates a decrease in brittleness (ductility increase) of the layers along with decreasing  $h$ . Such changes may be related to a decrease of the average crystallite size and microstrain in this case (see Fig. 18, b). In this case, the critical load value is determined by a decisive role of coating hardness value, which with the increase of thickness of the layers varied from 23 to 35 GPa.

Along with this, the most ductile form of wear (see Fig. 19) is characteristic for the coatings obtained at low pressure and reducing the nitrogen content, which determines strong covalent interatomic bonds. The hardness of these coatings is 4–7 GPa.

Summary data on the critical load abrasion of the coatings  $L_{C5}$  shown in Table 5 for the coatings produced at  $P_N = 3 \cdot 10^{-3}$  Torr and  $U_b = -300$  V show that the adhesion strength is great for all layer thicknesses of

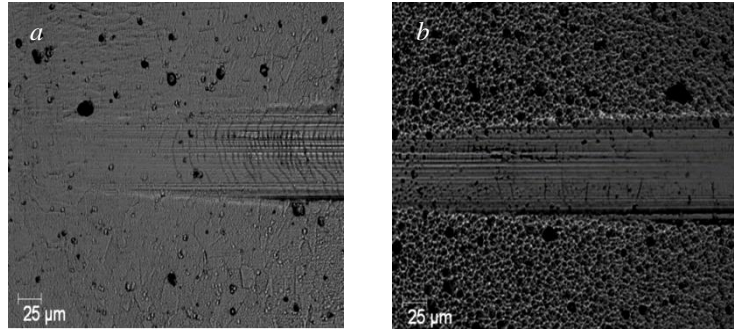


**Fig. 19.** Wear tracks at critical loads  $L_{C1}$  for the coatings produced at  $P_N = 7 \cdot 10^{-4}$  Torr (a) and  $P_N = 2 \cdot 10^{-4}$  Torr (b) [19].

**TABLE 5.** Critical load  $L_{C5}$  for the coatings obtained at  $P_N = 3 \cdot 10^{-3}$  Torr,  $U_b = -300$  V and different thickness of layers.

The thickness of layers $h$ , nm	$L_{C5}$ , N
13	130.9
25	152.1
50	156.7
100	157.3
200	185.7
400	187.6

such coatings, however, the increase in the thickness and hardening allows reaching the maximum value  $L_{C5} = 185\text{--}187$  N at the thicknesses of the layers of 200–400 nm.

It should be noted that for the initial stage of wear, the critical load for the coatings produced at  $P_N = 3 \cdot 10^{-3}$  Torr is in the range of 13–18 N, whereas for the plastic coatings obtained at low pressure of nitrogen atmosphere, the value  $L_{C1}$  is much lower, and has values of 6 and 4 N, respectively, for  $P_N = 7 \cdot 10^{-4}$  Torr and  $P_N = 2 \cdot 10^{-4}$  Torr.

#### 2.4. Metal Nitride (Group VI) Coatings

The studies of morphology of growth of the multilayer coatings showed their sufficiently large homogeneity and planarity in all the used modes for both types of (TiZrNbTaHf + Mo)N and (TiZrNbTaHf + W)N systems. The drop inhomogeneity was revealed on the surface, which did not lead to a significant change in planarity and average thickness (less than 0.5%, see the data on thickness in Fig. 20).

The analysis of element composition (EDX method) has shown that the increase of negative bias potential ( $U_b$ ) led to depletion of the coat-

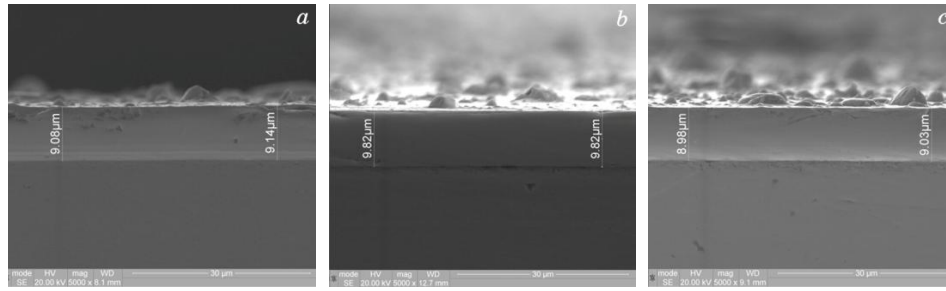


**Fig. 20.** SEM-pictures of the side surface of the ‘coating-substrate’ of the multilayer coatings: *a*—(TiZrNbTaHf)N/WN ( $P_N = 4 \cdot 10^{-3}$  Torr,  $U_b = -90$  V), *b*—(TiZrNbTaHf)N/MoN ( $P_N = 4 \cdot 10^{-3}$  Torr,  $U_b = -50$  V), *c*—(TiZrNbTaHf)N/MoN ( $P_N = 1.5 \cdot 10^{-3}$  Torr,  $U_b = -50$  V) [18].

ing by light atoms. The main reason of this is selective spraying of light atoms during the spraying from the surface of growth [12]. To the largest extent it affects nitrogen atoms, the content of which in the coating with the increase of  $U_b$ , in the studied range decreases more than 1.5 times (see Fig. 21).

It is worth noting, that at the same time saturation of the coatings (TiZrNbTaHf)N/WN with nitrogen is larger in comparison with (TiZrNbTaHf)N/MoN by modulus. In addition, the spray character (secondary selective spraying) is, apparently, a basis of change of metal components of layers.

In (TiZrNbTaHf)N/WN coatings, in the layers with WN, with the increase of  $U_b$  from  $-90$  to  $-280$  V, the content of heavy W (with respect to the content of metal elements in TiZrNbTaHf layer) increases from 33% to 53%.

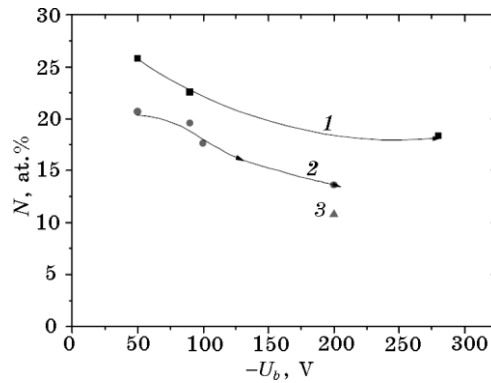


**Fig. 21.** Dependence of nitrogen atoms’ content in the coating on the value of ( $-U_b$ ): 1—(TiZrNbTaHf)N/WN ( $P_N = 4 \cdot 10^{-3}$  Torr), 2—(TiZrNbTaHf)N/MoN ( $P_N = 4 \cdot 10^{-3}$  Torr), 3—(TiZrNbTaHf)N/MoN ( $P_N = 1.5 \cdot 10^{-3}$  Torr) [18].

For the coatings (TiZrNbTaHf)N/MoN, the ratio between the atomic contents of Mo and metal of the second layer (TiZrNbTaHf) with the increase of  $U_b$  is practically not observed, remaining at a level of 41–42 at.% by its magnitude (Fig. 22, *a, c*) shows typical energy-dispersive spectra of the coatings and calculated atomic composition).

Annealing practically does not change the ratio of metal components and leads to a substantial change in content of nitrogen atoms of nitrogen and impurity oxygen atoms in the coating.

If, at a low bias potential, the content by nitrogen atoms is decreased by the absolute value by a value of about 2% (Fig. 22, *a, b*), than in the case of large  $U_b = -200$  V, the decrease is more significant and is 5% (Fig. 22, *c, d*). This can be linked with the additional formation of paths of light diffusion during the formation of solid solution of HEA atoms Mo(W) a boundary area because of radiation stimulated mixing.

The effect of bias potential and the pressure of working nitrogen atmosphere also greatly influenced phase composition and structural state of the coatings.

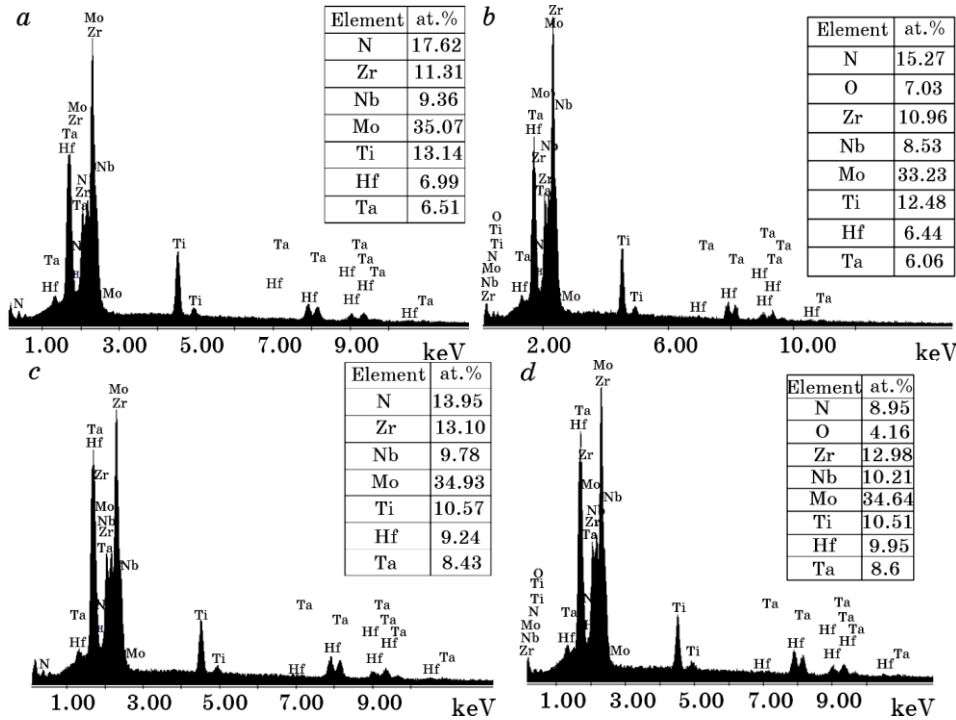


Fig. 22. Energy-dispersion spectra and element contents calculated by it in the coatings (TiZrNbTaHf)N/MoN ( $P_N = 4 \cdot 10^{-3}$  Torr) obtained at (a)  $-U_b = -100$  V (before the annealing), (b)  $-100$  V (after the annealing), (c)  $-200$  V (before the annealing), (d)  $-200$  V (after the annealing) [18].

Areas of X-ray diffraction spectra of the coatings, obtained under different technological conditions are shown in Fig. 23.

For comparison, the spectra of the coating before the annealing and after the high temperature vacuum annealing are shown in one figure for comparison.

The analysis of the obtained diffraction spectra shows that for all deposition modes the formation of phases with cubic (f.c.c.) lattice occurs in both layers of multilayer coatings.

In the layers of high-entropy alloy, it is a disordered solid solution (TiZrNbTaHf)N with the crystal lattice of NaCl type [22], in the layers of the Mo–N system, it is  $\gamma$ -Mo<sub>2</sub>N, but in the layers of the W–N system, it is  $\beta$ -W<sub>2</sub>N (PDF 25–1257). The similarity of structural states in the layers based on high entropy alloy and nitrides of VI Group transition metals (close relation of preferred orientation of crystallites layers) indicates the relationship between structure of layers and their growth.

From the obtained spectra, it can also be seen that in the coatings received during the deposition at low  $U_s$ , the post-condensation annealing does not lead to a significant change of the type of diffraction spec-

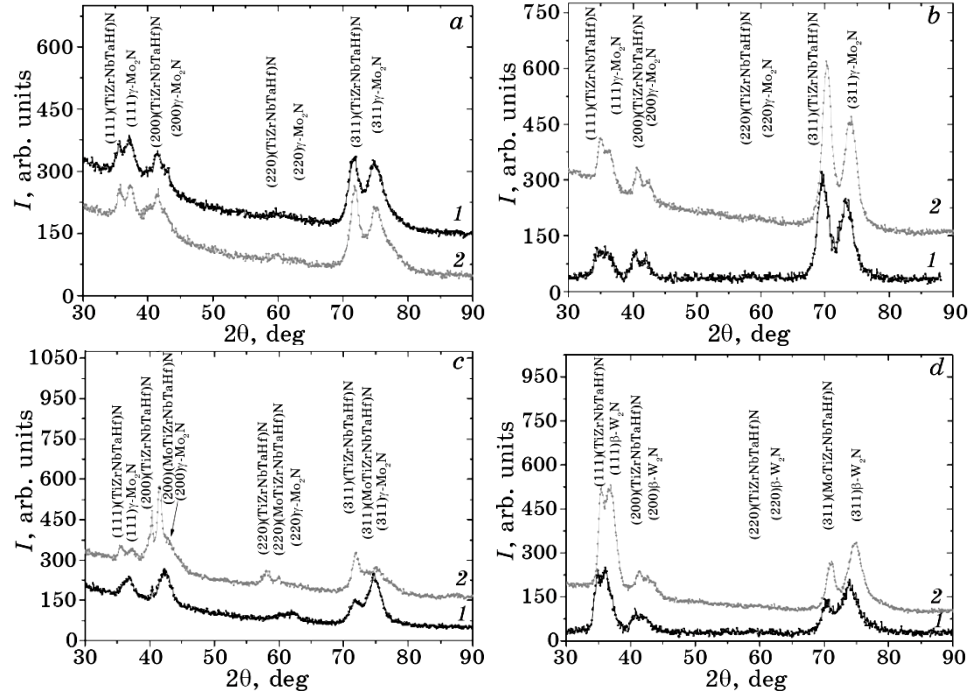


**Fig. 23.** Areas of X-ray diffraction spectra of (TiZrNbTaHf)N/MoN coatings: *a*— $P_N = 1.5 \cdot 10^{-3}$  Torr,  $-U_b = 50$  V; *b*— $P_N = 4 \cdot 10^{-3}$  Torr,  $-U_b = 50$  V; *c*— $P_N = 4 \cdot 10^{-3}$  Torr,  $U_b = -200$  V; and *d*—(TiZrNbTaHf)N/WN,  $P_N = 4 \cdot 10^{-3}$  Torr,  $-U_b = 90$  V. 1—after the annealing, 2—before the annealing at 700°C [18].

tra (let's compare 1 and 2 on the Fig. 23, *a, b, c, d*). During the increase of pressure of the working nitrogen atmosphere, the increase of texturing rate occurs (relative increase of intensity of reflexes). Thus, under relatively low values of  $U_s$ , in the (TiZrNbTaHf)N/MoN coatings, such a texture has an axis [311] (Fig. 23, *a, b*).

Applying a large negative potential  $U_b = -200$  V leads to an increase in the degree of 'chaotization' of the structure (the structure inherent to small  $U_s$  is not manifested for high  $U_s$ ), as well as to increase of dispersion of crystalline formations in the layers of the coatings, which is manifested the most for the layers  $\gamma$ -Mo<sub>2</sub>N for which with the increase of  $U_s$  the average size of crystallites decreases from 54 nm to 37 nm. For the coatings (TiZrNbTaHf)N/WN, the formation of texture with the axis [111] (Fig. 23, *d*) occurs at relatively low  $U_b = -90$  V, which is typical for the preferred minimization of deformation in the process of growth, the degree of perfection of which increases (spectrum 2 in Fig. 23, *d*) during the annealing. At the same time, reduction of the period of a lattice is observed in the annealed coatings in both layers: in (TiZrNbTaHf)N from 0.443 nm to 0.439 nm, and in  $\beta$ -W<sub>2</sub>N layers from 0.425 nm to 0.421 nm.

In the coatings (TiZrNbTaHf)N/MoN, annealing leads to a significant change of the lattice parameter almost exclusively in the nitride layers of high entropy alloy. The layers of the Mo-N system are characterized by the slight change of the grating period remaining at a range of 0.418–0.419 nm in the coatings obtained at low  $P_N = 1.5 \cdot 10^{-3}$  Torr and at the level of 0.425–0.424 nm at  $P_N = 4 \cdot 10^{-3}$  Torr. An exception is the coating obtained with a large  $U_s = -200$  V, for which even at  $P_N = 4 \cdot 10^{-3}$  Torr grating period does not exceed 0.420 nm. One more characteristic feature of this type of the coatings is formation of nitride phases of high-entropy alloy with a smaller period. Therefore, if the main nitride phase in the layers has a period of 0.44–0.47 nm, in the case of high values of applied  $U_b = -200$  V, the formation of a new fine crystalline phase occurs. It is manifested on the diffraction spectra before the annealing in the asymmetry of reflexes (see spectre 1 in Fig. 23, *c*), which in case of annealed coatings is found in the form of independent reflections from lattice planes of the phase with a period of 0.434–0.435 nm (see spectre 2 in Fig. 23, *c*).

Presumably, this effect may be associated with the formation of mixed solid solution phase based on the high entropy nitride of the type (MoTiZrNbTaHf)N (including Mo atoms from the second layer as a compound element) on a disordered interphase border. Formation of such a layer may lead to a decrease of functional properties of the coating and, in particular, mechanical properties.

The universal mechanical characteristics taking in account their sufficient ease of definition and good reproducibility are microindentation data and scratch testing.

The coatings of the greatest firmness according to the microindentation data are the coatings deposited at a relatively low potential bias. For the coatings (TiZrNbTaHf)N/WN, the hardness reaches 44 GPa, and for (TiZrNbTaHf)N/MoN, 41 GPa.

When increasing  $U_b$ , the hardness slightly falls down to 39 GPa, apparently due to the radiation-stimulated mixing. The pressure reduction also leads to a decrease in hardness.

In the case of the coatings obtained at low  $-U_b$ , post-condensation annealing leads to increase of hardness of such coatings because of ordering at high temperatures in high entropy nitride layers. To the greatest extent, it affects the coatings (TiZrNbTaHf)N/WN obtained at  $U_b = -90$  V, where the hardness increases from 44 GPa to 59 GPa. In the case of coatings (TiZrNbTaHf)N/MoN, the largest increase in hardness is observed at  $U_b = -50$  V: from 40.5 GPa before the annealing to 48.5 GPa after the annealing.

For the coatings obtained at large  $U_b \in [-280, -200]$  V, the annealing is followed by a slight not only leads to increased hardness, but also accompanied by a slight drop of hardness from 39–40 GPa before the annealing to 38–37 GPa after the annealing.

Results of scratch tests also show that the greatest pressure prior to the

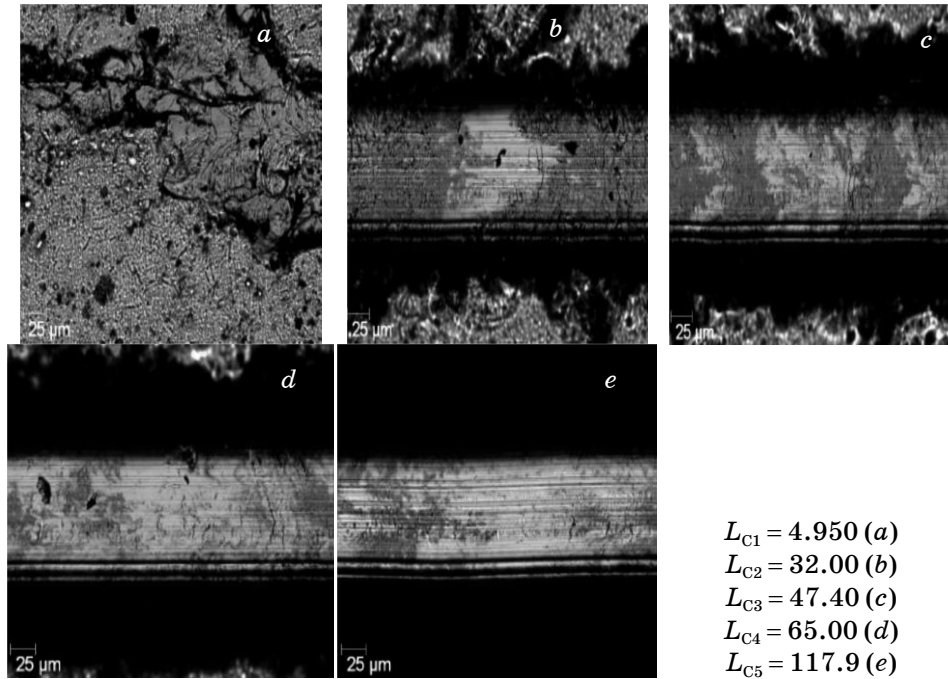


**Fig. 24.** View of wear tracks and the resulting critical loads for the coatings (TiZrNbTaHf)N/MoN ( $P_N = 4 \cdot 10^{-3}$  Torr,  $U_b = -150$  V) [18].

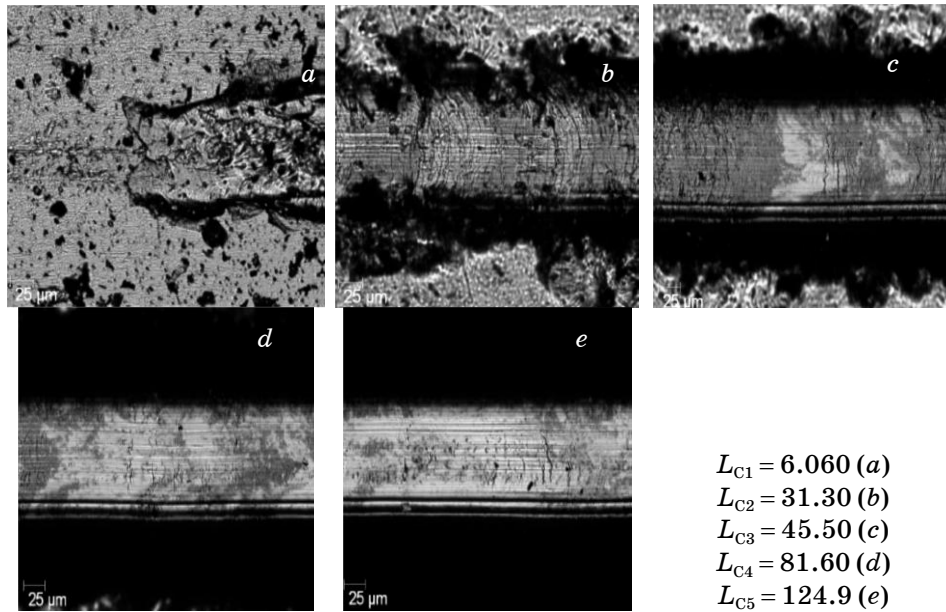


Fig. 25. View of wear tracks and the resulting critical loads for the coatings (TiZrNbTaHf)N/MoN (TiZrNbTaHf)N/WN ( $P_N = 4 \cdot 10^{-3}$  Torr,  $U_b = -90$  V) [18].

failure is inherent to the coatings obtained at low values of  $U_b$  and, for the coatings (TiZrNbTaHf)N/WN, reaches the values  $L_{C5} = 117.9$  N (Fig. 24), and for the coatings (TiZrNbTaHf)N/MoN,  $L_{C5} = 124.9$  N (Fig. 25).

The annealing at  $700^\circ\text{C}$  of the coatings of (TiZrNbTaHf)N/MoN system obtained at  $P_N = 3 \cdot 10^{-3}$  Torr,  $U_b = -150$  V, for which the initial hardness was relatively high (35 GPa), which then increased to 41.5 GPa after the annealing led to enhanced wear resistance for all values  $L_C$  (see Figs. 24, 25), and the wear is inherent to abrasion, which is manifested by the absence of large amplitude peaks (which are inherent to brittle failure) on the curve of dependence of acoustic emission on pressure (see Fig. 26, a).

Slightly larger by its magnitude hardness (48.5 GPa) of the composite coating (TiZrNbTaHf)N/MoN obtained at  $P_N = 4 \cdot 10^{-3}$  Torr and  $U_b = -50$  V after the annealing increases the critical values of  $L_{C1}$ ,  $L_{C2}$  and  $L_{C3}$  (see Figs. 24, 25), but, at the same time, the values of  $L_{C4}$  and  $L_{C5}$  are decreased, *i.e.* critical stresses responsible for the formation of multiple cracks and wear of material of the coating takes place.

The effect of formation of multiple cracks and brittle fracture of high hardness coating is observed even better for a steel-based substrate with a higher plasticity for the system (TiZrNbTaHf)N/WN, obtained at  $P_N = 4 \cdot 10^{-3}$  Torr,  $U_b = -90$  V, the hardness of which is increased as a result of annealing up to 59 GPa. In this case, the increase

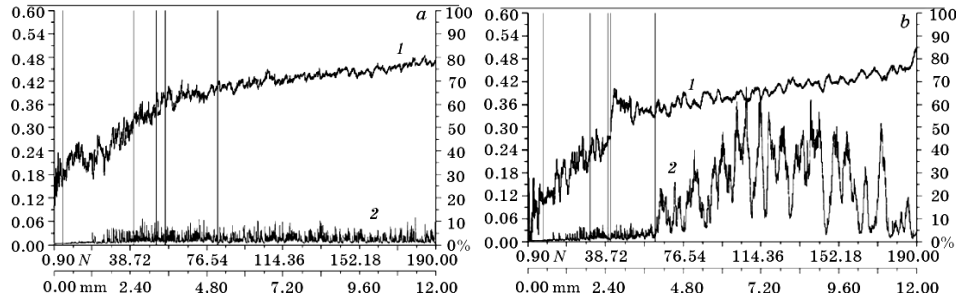


**Fig. 26.** Changes in average values of the coefficient of friction (spectrum 1, left scale) and in the amplitude of acoustic emission (spectrum 2, right scale) for the coatings: *a*—(TiZrNbTaHf)N/MoN ( $P_N = 4 \cdot 10^{-3}$  Torr,  $U_s = -150$  V) and *b*—(TiZrNbTaHf)N/WN ( $P_N = 4 \cdot 10^{-3}$  Torr,  $U_b = -90$  V) [18].

of value of the critical load  $L_{C1}$  (see Figs. 24, 25) takes place only, a slight relative decrease of  $L_{C2}$  and  $L_{C3}$  and a strong decrease of  $L_{C4}$  and  $L_{C5}$ . It is significant that in this area, strong peaks typical to the formation of macroareas with brittle failure appear on the dependence of the acoustic emission signal on the load (Fig. 26, *b*).

Thus, the achievement of ultrahigh hardness in a case of relatively ductile substrate may not lead to an increase in adhesive strength due to the brittle fracture of the coating during the wear process in the boundary areas to the ductile base material.

To determine tribological characteristics, the testing ‘ball–disc’ scheme was used, for which the balls with diameter of 6.0 mm made of sintered certified materials,  $Al_2O_3$  and steel  $Ac_{100}Cr_6$ , were used.

Visually, friction tracks (see Fig. 27) are characterized by the ab-

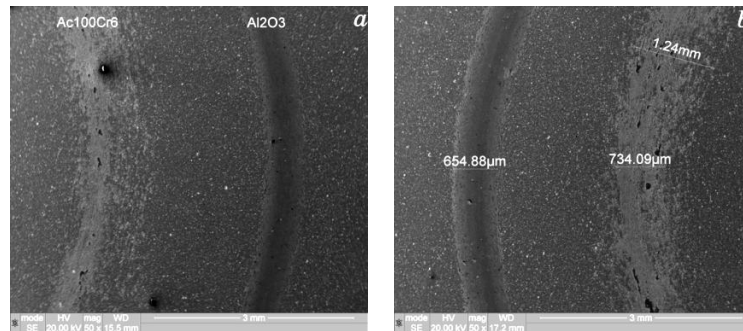


**Fig. 27.** Images of friction tracks during the tests (by the ‘ball–disc’ scheme with a counterbody (ball) made of  $Al_2O_3$  and steel  $Ac_{100}Cr_6$ ) of the multilayer coating (TiZrNbTaHf)N/MoN ( $P_N = 4 \cdot 10^{-3}$  Torr,  $U_b = -50$  V). *a*—with detailed friction tracks by the type of the counterbody, *b*—with the determined average sizes of friction tracks for different counterbodies [18].

**TABLE 6.** The critical load  $L_C$  for composite multilayer coatings, before and after one-hour annealing at 700°C.

Coating type	$-U_b$ , V	Annealing, °C	$L_C$ , N				
			1	2	3	4	5
(TiZrNbTaHf)N/MoN	150	–	4.52	31.8	48.2	65.8	73.1
		700	5.07	40.2	51.4	56.0	82.2
(TiZrNbTaHf)N/MoN	50	–	6.06	31.3	45.5	81.6	124.9
		700	7.33	42.8	58.4	63.8	81.7
(TiZrNbTaHf)N/WN	90	–	4.95	32.0	47.4	65.0	117.9
		700	8.31	31.3	39.7	41.3	62.7

sence of barbs, chips, and radial cracks, which indicates the high quality of the coating and its adhesive strength.

The average width of the friction track in a case of the counterbody made of  $\text{Al}_2\text{O}_3$  has a value of 654.88  $\mu\text{m}$  (see Fig. 27, *b*), and in the case of steel counterbody, the track has different thickness and is characterized by a non-uniform wear pattern.

The reason for this heterogeneous nature is sticking of relatively soft and ductile metal of the counterbody to the coating, which increases the actual impact area, and further friction occurs in a pair of worn-out metal and the metal of counterbody.

Lowering of the fixed friction coefficient and increase of wear of a steel ball is also linked with this (Table 6).

During friction with a counterbody made of  $\text{Al}_2\text{O}_3$ , the uniform abrasive wear of the friction pair with the removal of wear products and their accumulation at the edges of the groove was observed (Fig. 27, *a*).

In this case, the amount of transferred material depends on the strength of adhesive bond, which depends on the electronic structure of the counterbody based on  $\text{Al}_2\text{O}_3$  and multilayer coating, and determines the ability to form solid solutions, intermetallic compounds with each other, and oxides stable at high temperatures. This is related to the high values of the coefficient of friction during the tests with  $\text{Al}_2\text{O}_3$  counterbody, which include high entropy nitride (TiZrHfVNbTa)N [14].

At the same time, the coatings possess good wear resistance: wear value for both types of counterbodies is within the limits  $(0.39\text{--}2.12)\cdot 10^{-5} \text{ mm}^3 \times \text{N}^{-1} \times \text{mm}^{-1}$ . Wear of the counterbody of  $\text{Al}_2\text{O}_3$  is also sufficiently small— $2.25 \cdot 10^{-6} \text{ mm}^3 \times \text{N}^{-1} \times \text{mm}^{-1}$  (Table 7), in contrast with a steel counterbody  $\text{Ac}_{100}\text{Cr}_6$ , for which wear differs by one order and has a value of  $2.59 \cdot 10^{-4} \text{ mm}^3 \times \text{N}^{-1} \times \text{mm}^{-1}$ .

Thus, a universal resistance of multilayer coatings based on nitrides of high entropy alloys to various types of counterbodies, different in hardness and toughness opens good perspectives to use such coatings as protective coatings at complex exposures in conditions of abrasive wear [1, 15].

**TABLE 7.** Tribological characteristics of the multilayer (TiZrNbTaHf)N/MoN coating ( $P_N = 4 \cdot 10^{-3}$  Torr,  $U_b = -50$  V) during the tests by the scheme ‘ball-disc’ with counterbody (ball) of  $\text{Al}_2\text{O}_3$  and steel  $\text{Ac}_{100}\text{Cr}_6$ .

Type of counterbody	Coefficient of friction	Wear factor, $\text{mm}^3 \times \text{N}^{-1} \times \text{mm}^{-1}$	
		Counterbody	Coated samples
$\text{Al}_2\text{O}_3$	0.83	$2.25 \times 10^{-6}$	$3.90 \times 10^{-6}$
$\text{Ac}_{100}\text{Cr}_6$ steel	0.57	$2.59 \times 10^{-4}$	$2.12 \times 10^{-5}$

### 3. CONCLUSIONS

In this article, the influence of the size of bilayers deposition parameters, the stress and microstructure of the change of physical and mechanical properties of the nanostructure (nanocomposite) coatings produced by vacuum arc deposition from the cathode is written and shown. Presented results are an intermediate stage of our work in the field of development and study of nanoscale multilayer coatings formed from refractory metals. The present results suggest the prospect of obtaining and studying such nanoscale nitride multilayer nanostructured coatings in the near future.

This work was done under the aegis of the State budget programs 0113U000137c ‘Physical principles of plasma technologies for complex treatment of multicomponent materials and coatings’, 0115 U000682 ‘The development of material science basis of a structural engineering, vacuum plasma superhard coatings in order to reach the required functional properties’ and in collaboration with the Institute ‘P’-Prime, University Poitiers France, National Institute for Materials Science, Tsukuba Ibasaki, Japan, and NBMC, Adam Mickiewicz University, Poland. The authors are grateful to co-authors of the original work (the basis of which composes this review), namely, O. V. Bondar, B. A. Postolnyi, V. A. Stolbovoy, V. Yu. Novikov, S. V. Lytovchenko, O. V. Sobol’, U. S. Nyemchenko, I. N. Toryanik, D. A. Kolesnikov and others.

### REFERENCES

1. A. D. Pogrebnjak and V. M. Beresnev, *Nanocoatings Nanosystems Nanotechnologies* (Sharyach: Bentham Sci. Publ.: 2012).
2. A. D. Pogrebnjak, D. Eyidi, G. Abadias, O. V. Bondar, V. M. Beresnev, and O. V. Sobol, *Int. J. Refract. Met. Hard. Mater.*, **48**: 222 (2015).
3. A. D. Pogrebnjak, I. V. Yakushchenko, A. A. Bagdasaryan, O. V. Bondar, R. Krause-Rehberg, G. Abadias, P. Chartier, K. Oyoshi, Y. Takeda, V. M. Beresnev, and O. V. Sobol, *Mater. Chem. Phys.*, **147**: 1079 (2014).
4. V. Ivashchenko, S. Veprek, A. Pogrebnjak, and B. Postolnyi, *Sci. Technol. Adv. Mat.*, **15**: 025007 (2014).
5. A. D. Pogrebnjak, A. P. Shpak, N. A. Azarenkov, and V. M. Beresnev, *Physics-*

- Uspekhi*, **52**: 29 (2009).
6. A. D. Pogrebnjak, *J. Nanomater.*, **2013**: 12 (2013).
  7. A. D. Pogrebnjak, A. P. Kobzev, B. P. Gritsenko, S. Sokolov, E. Bazyl, N. V. Sviridenko, A. N. Valyaev, and Y. F. Ivanov, *J. Appl. Phys.*, **87**: 2142 (2000).
  8. A. D. Pogrebnjak, V. M. Beresnev, A. A. Demianenko, V. S. Baidak, F. F. Komarov, M. V. Kaverin, N. A. Makhmudov, and D. A. Kolesnikov, *Phys. Solid State*, **54**: 1882 (2012).
  9. A. D. Pogrebnjak, V. N. Borysyuk, A. A. Baghdasaryan, O. V. Maksakova, and E. V. Smirnova, *J. Nano-Electron. Phys.*, **6**: 04018 (2014).
  10. V. M. Beresnev, O. V. Sobol', A. D. Pogrebnjak, P. V. Turbin, and S. V. Litovchenko, *Tech. Phys.*, **55**: 871 (2010).
  11. R. Krause-Rehberg, A. D. Pogrebnjak, V. N. Borysyuk, M. V. Kaverin, A. G. Ponomarev, M. A. Bilokur, K. Oyoshi, Y. Takeda, V. M. Beresnev, and O. V. Sobol', *Phys. Met. Metallogr.*, **114**: 672 (2013).
  12. A. D. Pogrebnjak, V. M. Beresnev, D. A. Kolesnikov, O. V. Bondar, Y. Takeda, K. Oyoshid, M. V. Kaverin, O. V. Sobol, R. Krause-Rehberg, and C. Karwatg, *Acta Phys. Pol. A*, **123**: 816 (2013).
  13. N. A. Azarenkov, O. V. Sobol, V. M. Beresnev, A. D. Pogrebnjak, D. A. Kolesnikov, P. V. Turbin, and I. M. Torianyk, *Metallofiz. Noveishie Tekhnol.*, **35**: 1061 (2013).
  14. S. N. Grigoriev, O. V. Sobol, V. M. Beresnev, I. V. Serdyuk, A. D. Pogrebnjak, D. A. Kolesnikov, and U. S. Nyemchenko, *J. Frict. Wear*, **35**: 359 (2014).
  15. A. D. Pogrebnjak, O. V. Bondar, N. K. Erdybaeva, S. V. Plotnikov, P. V. Turbin, S. S. Grankin, V. A. Stolbovoy, O. V. Sobol, D. A. Kolesnikov, and C. Kozak, *Prz. Elektrotechniczn.*, **12**: 228 (2015).
  16. B. O. Postolnyi, P. Konarski, F. F. Komarov, O. V. Sobol', O. V. Kyrychenko, and D. S. Shevchuk, *J. Nano-Electron. Phys.*, **6**: 04016 (2014).
  17. S. S. Grankin, V. M. Beresnev, O. V. Sobol, V. A. Stolbovoy, V. Yu. Novikov, S. V. Lytovchenko, U. S. Nyemchenko, A. A. Meylehov, M. G. Kovaleva, A. A. Postelnik, and I. N. Toryanik, *J. Nano-Electron. Phys.*, **7**: 04050 (2014).
  18. U. S. Nyemchenko, V. M. Beresnev, O. V. Sobol, S. V. Lytovchenko, V. A. Stolbovoy, V. Ju. Novikov, A. A. Meylekhov, A. A. Postelnik, and M. G. Kovaleva, *Phys. Atom. Nucl.* (2015) (to be published).
  19. T. N. Kołtunowicz, P. Żukowski, V. Bondariev, J. A. Fedotova, and A. K. Fedotov, *Vacuum*, **120**: 37 (2015).
  20. A. V. Khomenko, I. A. Lyashenko, and V. N. Borysyuk, *Ukr. J. Phys.*, **54**: 1139 (2009).
  21. O. V. Sobol', A. A. Andreev, V. A. Stolbovoi, and V. F. Fil'chikov, *Techn. Phys. Lett.*, **38**: 168 (2012).
  22. L. Chen, S. Q. Wang, S. Z. Zhou, J. Li, and Y. Z. Zhang, *Int. J. Refract. Met. H.*, **26**: 456 (2008).
  23. O. V. Sobol, A. A. Andreev, S. N. Grigoriev, V. F. Gorban, M. A. Volosova, S. V. Aleshin, and V. A. Stolbovoy, *Met. Sci. Heat Treat.*, **54**: 195 (2012).
  24. K. J. Kadhim, N. Abd Rahman, M. R. Salleh, and K. I. Mohd Zukee, *Appl. Mech. Mater.*, **761**: 417 (2015).
  25. C. Harish Barshilia, Anjana Jain, and K. S. Rajam, *Vacuum*, **72**: 241 (2004).
  26. O. V. Sobol', *Phys. Solid State*, **53**: 1464 (2011).
  27. O. M. Ivasishin, A. D. Pogrebnjak, and S. N. Bratushka, *Nanostructured Layers and Coating Formed by Ion-Plasma Fluxes in Titanium Alloys and Steels*

- (Kyiv: Akadempriodika: 2011).
28. Q. Meng, M. Wen, P. Liu, K. Zhang, and W. Zheng, *Mater. Lett.*, **94**: 61 (2013).
  29. H. Soderberg, M. Oden, T. Larsson, L. Hultman, and J. M. Molina Aldareguia, *Appl. Phys. Lett.*, **88**, No. 19: 191902-1 (2006).
  30. A. D. Pogrebnjak, *Mater. Sci. Appl.*, **4**, No. 4A: 24 (2013).
  31. M. Wen, Q. Meng, C. Hu, T. Au, Y. Su, W. Yu, and W.T. Zheng, *Surf. Coat. Technol.*, **203**: 1702 (2009).
  32. J. Lao, N. Shao, F. Mei, Li G, and M. Gu, *Appl. Phys. Lett.*, **86**: 011902-1 (2005).
  33. M. Setoyama, A. Nakayama, M. Tanaka, N. Kitagawa, and T. Nomura, *Surf. Coat. Technol.*, **86–87**: 225 (1996).
  34. G. Gassner, Ph. Mayrhofer, K. Kutschey, C. Mitterer, and M. Kathrei, *Surf. Coat. Technol.*, **201**: 3335 (2006).
  35. A. D. Pogrebnjak, S. N. Bratushka, V. I. Boyko, I. V. Shamanin, and Yu. V. Tsvintarnaya, *Nucl. Instr. Meth. Phys. Res. B*, **145**, No. 3: 373 (1998).
  36. M. Nordin, M. Larsson, and S. Hogmark, *Surf. Coat. Technol.*, **106**: 234 (1998).
  37. J. Musil, *Surf. Coat. Technol.*, **207**: 50 (2012).
  38. I. N. Martev, D. A. Dechev, N. P. Ivano, Ts. D. Uzunov, and E. P. Kashchieva, *J. Phys. Conf. Ser.*, **223**, No. 1: 012 (2010).
  39. A. D. Pogrebnjak, O. V. Sobol, V. M. Beresnev, P. V. Turbin, G. V. Kirik, N. A. Makhmudov, V. Ilyashenko, A. P. Shpylenko, M. V. Kaverin, M. Yu. Tashmetov, and A. V. Pshyk, *Nanostructured Materials and Nanotechnology IV: Ceramic Engineering and Science Proceedings*, **31**, No. 7: 127 (2010).
  40. A. Bendavid, P. J. Martin, X. Wang, M. Wittling, and T. J. Kinder, *J. Vac. Sci. Technol. A*, **13**, No. 3: 1658 (1995).
  41. K. R. Kazdaev, R. B. Abylkalykova, and L. I. Kveglis, *J. Sib. Fed. Univ. Eng. Technol.*, **5**: 560 (2012).
  42. H. W. Yen, C. Y. Huang, and J. R. Yang, *Scr. Mater.*, **61**: 616 (2009).
  43. D. Machon, D. Daisenberger, E. Soignard, E. Shen, T. Kawashima, E. Takayama-Muromachi, and P. F. McMillan, *Phys. Stat. Solid. A*, **203**, No. 5: 831 (2006).
  44. *Chemical Vapor Deposition: Precursors, Processes and Applications* (Eds. A. Jones and M. L. Hitchman) (Cambridge: RSC Publishing: 2009).
  45. J. S. Koehler, *Phys. Rev. B*, **2**, No. 2: 547 (1970).
  46. G. Zhang, F. Tianxiang, W. Tao, and C. Hailin, *Appl. Surf. Sci.*, **274**: 231 (2013).
  47. A. D. Pogrebnjak, V. M. Beresnev, O. V. Bondar, G. Abadias, P. Chartier, B. A. Postolnyi, A. A. Andreev, and O. V. Sobol, *Tech. Phys. Lett.*, **40**, No. 3: 215 (2014).
  48. J. Musil, P. Novak, M. Hromadka, R. Cerstvy, Z. Soukup, and J. Savkova, *Surf. Coat. Technol.*, **215**: 386 (2013).
  49. N. I. Poliak, V. M. Anishchik, N. G. Valko, C. Karwat, C. Kozak, and Opielak, *Acta Phys. Pol. A*, **125**, No. 6: 1415 (2014).
  50. T. N. Koltunowicz, P. Zhukowski, V. Bondariev, A. Saad, J. A. Fedotova, A. K. Fedotov, M. Miloslavljivic, and J. V. Kasiuk, *J. Alloys Compd.*, **615**, No. 1: S361 (2014).
  51. I. A. Svito, J. A. Fedotova, M. Miloslavljivic, P. Zhukowski, N. T. Koltunowicz, A. Saad, K. Kierczynski, and A. K. Fedotov, *J. Alloys Compd.*, **615**, No. 1: S344 (2014).